

Generalized Liquid Association Analysis for Multimodal Data Integration

Lexin Li[†], Jing Zeng[‡], and Xin Zhang[‡] *

[†]*University of California at Berkeley* and [‡]*Florida State University*

Abstract

Multimodal data are now prevailing in scientific research. A central question in multimodal integrative analysis is to understand how two data modalities associate and interact with each other given another modality or demographic covariates. The problem can be formulated as studying the associations among three sets of random variables, a question that has received relatively less attention in the literature. In this article, we propose a novel generalized liquid association analysis method, which offers a new and unique angle to this important class of problem of studying three-way associations. We extend the notion of liquid association of Li (2002) from the univariate setting to the multivariate and high-dimensional setting. We establish a population dimension reduction model, transform the problem to sparse Tucker decomposition of a three-way tensor, and develop a higher-order singular value decomposition estimation algorithm. We derive the non-asymptotic error bound and asymptotic consistency of the proposed estimator, while allowing the variable dimensions to be larger than and diverge with the sample size. We demonstrate the efficacy of the method through both simulations and a multimodal neuroimaging application for Alzheimer's disease research.

Key Words: Liquid association; Multimodal neuroimaging; Sufficient dimension reduction; Tensor analysis; Tucker tensor decomposition.

*The authors contributed equally to this work and are listed in alphabetical order.

1 Introduction

1.1 Motivation and problem formulation

Multimodal data are now prevailing in scientific research, where different types of data, based on different physical and physiological sensitivities of machines and technologies, are acquired for a common set of experimental subjects. One example is multi-omics, where different genetic information such as gene expressions, copy number alternations, and methylation changes are jointly collected for the same biological samples (Richardson et al., 2016). Another example is multimodal neuroimaging, where distinct brain characteristics including brain structure, function, and chemical constituents are simultaneously measured for the same study subjects (Uludag and Roebroek, 2014). Integrative analysis of multimodal data aggregates such diverse and often complementary information, and consolidates knowledge across multiple data modalities.

In this article, we aim to address a question of central interest in multimodal integrative analysis, i.e., to understand how different data modalities associate and interact with each other given other modalities or demographic covariates. Our motivation is a multimodal positron emission tomography (PET) study for Alzheimer’s disease (AD) research. Amyloid-beta and tau are two hallmark proteins of AD, and both can be measured in vivo by PET imaging using different nuclear tracers. The two proteins are closely associated in terms of spatial patterns of their accumulations, and such association patterns are believed to be highly affected by the subject’s age (Braak and Braak, 1991). On the other hand, their specific age-dependent regional associations remain unclear. The data we study involve 81 elderly subjects, each receiving two PET scans that measure the depositions of amyloid-beta and tau, respectively. Each PET modality is represented by a vector of measurements recording the amount of the protein at a set of parcellated brain regions-of-interest. Brain parcellation is particularly useful to facilitate the interpretation, and has been frequently employed in brain imaging analysis (Fornito et al., 2013; Kang et al., 2016). We focus on the brain regions known to have possible amyloid-beta and tau accumulations. This results in 60 regions for amyloid-beta, and 26 regions for tau. Our goal is to find how and where in the brain the associations of the two proteins are the most contrastive as age varies.

This problem can be formulated statistically as studying the associations of two sets of random variables $\mathbf{X} \in \mathbb{R}^{p_1}$ and $\mathbf{Y} \in \mathbb{R}^{p_2}$ conditional on the third set of random variables $\mathbf{Z} \in \mathbb{R}^{p_3}$. In our example, \mathbf{X} denotes the amyloid-beta PET imaging with $p_1 = 60$, \mathbf{Y} denotes the tau

PET imaging with $p_2 = 26$, and \mathbf{Z} denotes the subject’s age with $p_3 = 1$. Meanwhile, in plenty of multimodal applications, \mathbf{X} , \mathbf{Y} , \mathbf{Z} can all be high-dimensional, and their dimensions can be even larger than the sample size. For instance, in imaging genetics (Nathoo et al., 2017), \mathbf{X} , \mathbf{Y} can represent different imaging modalities, whose dimensions can be in hundreds, and \mathbf{Z} can denote the genetic information, whose dimension can be in tens of thousands or more. In high-dimensional data analysis, it is common to postulate that the data information can be sufficiently captured by some low-dimensional representations, or most often, some linear combinations of the originally high-dimensional variables (Cook, 2007). Adopting this view, our question can be formulated as seeking linear combinations of \mathbf{X} and linear combinations of \mathbf{Y} whose conditional associations given \mathbf{Z} are the most contrastive. In other words, we seek linear combinations of \mathbf{X} and \mathbf{Y} that change the most as \mathbf{Z} changes.

We also comment that, although motivated by a specific multimodal neuroimaging study, the problem we address is of a broad scientific interest, and the method is applicable to other multimodal studies, e.g., the multi-omics data analysis (Shen et al., 2013).

1.2 Related work

There has been a rich statistical literature studying the associations between two sets of multivariate variables \mathbf{X} and \mathbf{Y} . A well studied and commonly used family of methods are canonical correlation analysis (CCA) and its variants (Witten et al., 2009; Gao et al., 2015; Li and Gaynanova, 2018; Shu et al., 2019; Mai and Zhang, 2019, among others). CCA explores the symmetric relations between \mathbf{X} and \mathbf{Y} , and looks for pairs of linear combinations that are most correlated. This goal, however, is different from ours, as the highly correlated linear combinations of \mathbf{X} and \mathbf{Y} are not necessarily the ones that are the most contrastive. For instance, a pair of linear combinations of \mathbf{X} and \mathbf{Y} can be highly correlated, while this correlation remains a constant as the value of \mathbf{Z} varies, and as such they are not the target of our problem. We later numerically compare our method with CCA to further demonstrate their differences. Another popular family of methods are sufficient dimension reduction (SDR), which looks for linear combinations of \mathbf{X} that capture full regression information of \mathbf{Y} given \mathbf{X} ; see the recent book of Li (2018) for a comprehensive review of this topic. Later we show that our proposed method is connected to several SDR methods, including principal Hessian directions (Li, 1992; Cook, 1998; Tang et al., 2020), and partial and groupwise sufficient dimension reduction (Chiaromonte et al., 2002; Li et al., 2010).

However, the goals of the two are utterly different. Whereas SDR studies asymmetric relations of \mathbf{Y} conditioning on \mathbf{X} , we seek symmetric relations between \mathbf{X} and \mathbf{Y} conditioning on the third set of variables \mathbf{Z} , in that the roles of \mathbf{X} and \mathbf{Y} are interchangeable, but not with the role of \mathbf{Z} .

Compared to the setting of two sets of variables, there have been much fewer statistical methods studying the associations among three sets of multivariate variables in the form of \mathbf{X} and \mathbf{Y} given \mathbf{Z} . In his groundbreaking work, Li (2002) proposed a novel three-way interaction metric, termed *liquid association*, that measures the extent to which the association of a pair of random variables depends on the value of a third variable. He showed that this metric is particularly useful in discovering co-expressed gene pairs that are regulated by another gene. However, Li (2002) only considered the scenario where all three variables X, Y, Z are one-dimensional. Li et al. (2004) extended the notion of liquid association to the scenario of a multivariate \mathbf{X} and a scalar Z , and sought two linear combinations $\gamma_1^T \mathbf{X}$ and $\gamma_2^T \mathbf{X}$ such that $\text{corr}(\gamma_1^T \mathbf{X}, \gamma_2^T \mathbf{X} | Z)$ varies the most with Z . Ho et al. (2011) and Yu (2018) developed some modified versions of liquid association, but still focused on the one-dimensional X, Y, Z scenario. Relatedly, Chen et al. (2011) proposed a bivariate conditional normal model to identify the variables that regulate the co-expression patterns between two genes. That corresponds to the scenario with a scalar X , a scalar Y and a multivariate \mathbf{Z} . Abid et al. (2018) proposed contrastive principal component analysis for a multivariate \mathbf{X} and a binary scalar Z , which sought linear combinations of \mathbf{X} that have the largest changes in the conditional variance given $Z = 0$ versus $Z = 1$. Moreover, Lock et al. (2013); Li and Jung (2017) developed a class of matrix and tensor factorization methods, which aimed to decompose the multimodal data into the components that capture joint variation shared across modalities, and the components that characterize modality-specific variation. Their goal is again different from ours, as their methods did not target the conditional distribution of \mathbf{X}, \mathbf{Y} given \mathbf{Z} . Finally, Xia et al. (2019) analyzed a similar dataset as our motivation example, but tackled a totally different problem. They studied hypothesis testing of covariance between the two multivariate PET measurements, and worked on the residuals after regressing out the age effect, which involves no conditioning of any third set of variables.

1.3 Proposal and contributions

In this article, we study the three-way associations among multivariate $\mathbf{X}, \mathbf{Y}, \mathbf{Z}$, and seek a set of linear combinations of \mathbf{X} and \mathbf{Y} that has a varying association as \mathbf{Z} varies. We generalize

the notion of liquid association of Li (2002) from the univariate case to the multivariate case. However, such a generalization is far from trivial, leading to a completely different estimation method and the associated asymptotic theory. For the estimation, we transform the generalized liquid association analysis to the problem of sparse Tucker decomposition of a three-way tensor, and introduce sparsity for the linear combinations to improve the interpretability. We then develop a higher-order singular value decomposition algorithm for parameter estimation. For the theory, we establish a population model that is essential for the study of statistical properties. We then derive the error bound and consistency, while allowing the variable dimensions p_1, p_2, p_3 to be larger than and to diverge to infinity along with the sample size n . As a result, our proposal makes some useful contributions from both the scientific and statistical perspectives.

Scientifically, characterizing the associations between different modalities given other modalities or covariates is of crucial importance for multimodal integrative analysis. However, there is almost no existing statistical solution available for this type of problem, especially when all the modalities involved are high-dimensional. Our proposal offers a unique angle for this important class of problem. As an illustration, for our multimodal PET study, understanding the dynamic patterns between amyloid-beta and tau with respect to age would offer pivotal insight about how pathological proteins of Alzheimer’s disease interact in the aging human brain. In turn, it could lead to better design and subject recruitment of clinical trials to potentially slow the spread of AD. For instance, clinical trials that aim at testing anti-amyloid-beta or anti-tau agents would need to know not only that participants have amyloid-beta and tau in the brain, but also how the relative levels of each pathological protein are spatially associated with each other given their ages.

Statistically, our proposal of generalized liquid association analysis makes a useful addition to the toolbox of association analysis of more than two sets of variables. Moreover, our method involves sparse tensor decomposition, which is itself of independent interest. Tensor data analysis is gaining increasing attention in recent years (Kolda and Bader, 2009; Zhou et al., 2013; Bi et al., 2018; Tang et al., 2019; Zhang and Han, 2019, among others); see also Bi et al. (2020) for a review of tensor analysis in statistics. Nevertheless, our proposal differs in several ways. Particularly, our sparse tensor decomposition algorithm is related to some recent proposals of singular value decomposition (SVD) for matrix denoising (Yang et al., 2016) and tensor denoising (Zhang and Han, 2019), in that they share a similar iterative hard thresholding SVD scheme. However, our algorithm is tailored to the tensor parameter estimation with more flexible initialization and

tuning. As a result, our theoretical analysis differs considerably from the denoising problems. Whereas both Yang et al. (2016) and Zhang and Han (2019) achieved the minimax optimal estimation for their denoising problems, we establish the dimension reduction subspace recovery consistency, variable selection consistency, and tensor parameter estimation consistency. Our rate of convergence matches the optimal rate in previous works, and all the consistency results are established in the ultra-high dimensional setting of $s \log(p) = o(n)$, where $s = s_1 s_2 s_3$ and $p = p_1 p_2 p_3$ are the products of the number of nonzero entries and dimensions, respectively, in \mathbf{X} , \mathbf{Y} and \mathbf{Z} . Our theoretical development is highly non-trivial, and may be of independent interest for future research involving tensor parameter estimation in a statistical model with i.i.d. data. In a sense, our work further broadens the scope of higher-order sparse SVD and tensor analysis.

The rest of the article is organized as follows. Section 2 develops the concept of generalized liquid association, and the corresponding population model of generalized liquid association analysis. Section 3 introduces the estimation algorithm, and Section 4 establishes the theoretical guarantees. Section 5 presents the simulations, and Section 6 revisits the multimodal PET study. Section 7 concludes the paper with a discussion, and the Supplementary Appendix collects all technical proofs and additional numerical results.

2 Generalized Liquid Association Analysis

2.1 Generalized liquid association

We begin with a brief review of the concept of liquid association (LA) proposed by Li (2002) for the univariate case. We then extend this notion to the multivariate case.

Suppose X, Y, Z are random variables with mean zero and variance one. Define $g(z) = E(XY|Z = z) : \mathbb{R} \mapsto \mathbb{R}$. Li (2002) defined the liquid association of X and Y given Z as,

$$\text{LA}(X, Y | Z) = E \left\{ \frac{dg(Z)}{dZ} \right\} = E \left\{ \frac{d}{dZ} E(XY | Z) \right\},$$

When Z follows a standard normal distribution, by Stein's Lemma (Stein, 1981), we have,

$$\text{LA}(X, Y | Z) = E \{g(Z)Z\} = E(XYZ).$$

Intuitively, $\text{LA}(X, Y | Z)$ characterizes the change of the association of X and Y conditioning on Z through $g(z)$, and the normality condition connects this quantity with the simple unconditional

expectation $E(XYZ)$. In practice, the univariate Z is transformed to standard normal using the normal score transformation, and the LA measure is estimated by the sample mean $E(XYZ)$. Li et al. (2004) considered an extension of LA to a multivariate $\mathbf{X} \in \mathbb{R}^{p_1}$ and a scalar Z , by looking for two linear combinations, such that $\text{LA}(\gamma_1^T \mathbf{X}, \gamma_2^T \mathbf{X} | Z) = \gamma_1^T E(\mathbf{X} \mathbf{X}^T Z) \gamma_2$ is maximized. It has a close-form solution that $\gamma_1 = (\mathbf{v}_1 + \mathbf{v}_p) / \sqrt{2}$, $\gamma_2 = (\mathbf{v}_1 - \mathbf{v}_p) / \sqrt{2}$, where \mathbf{v}_1 and \mathbf{v}_p are the eigenvectors of the matrix $E(\mathbf{X} \mathbf{X}^T Z) \in \mathbb{R}^{p \times p}$ with the largest and smallest eigenvalues.

We next extend the concept of liquid association to the multivariate case, where $\mathbf{X} \in \mathbb{R}^{p_1}$, $\mathbf{Y} \in \mathbb{R}^{p_2}$, and $\mathbf{Z} \in \mathbb{R}^{p_3}$. Without loss of generality, suppose each variable entry in \mathbf{X} , \mathbf{Y} , and \mathbf{Z} are standardized with mean zero and variance one. Define

$$\mathbf{g}(\mathbf{z}) = E(\mathbf{X} \mathbf{Y}^T | \mathbf{Z} = \mathbf{z}) : \mathbb{R}^{p_3} \mapsto \mathbb{R}^{p_1 \times p_2}.$$

We then define the generalized liquid association measure, which is a three-way tensor, as follows.

Definition 1. *The generalized liquid association (GLA) of \mathbf{X} and \mathbf{Y} with respect to \mathbf{Z} is,*

$$\Phi = \text{GLA}(\mathbf{X}, \mathbf{Y} | \mathbf{Z}) = E \left\{ \frac{d}{d\mathbf{Z}} \mathbf{g}(\mathbf{Z}) \right\} \in \mathbb{R}^{p_1 \times p_2 \times p_3}.$$

When \mathbf{Z} follows a multivariate normal distribution, by the multivariate version of Stein's lemma (Liu, 1994, Lemma 1), we have the following property regarding Φ .

Proposition 1. *If $\mathbf{Z} \sim \text{Normal}(0, \Sigma_{\mathbf{Z}})$, then $\Phi = E(\mathbf{X} \circ \mathbf{Y} \circ \mathbf{Z}) \times_3 \Sigma_{\mathbf{Z}}^{-1}$, where \circ denotes the outer product, and \times_3 denotes the mode-3 product between a tensor and a matrix.*

This extension from univariate to multivariate variables is straightforward. However, we recognize that all \mathbf{X} , \mathbf{Y} and \mathbf{Z} can be high-dimensional such that $p_1, p_2, p_3 > n$, and the dimension of Φ is the product $p_1 p_2 p_3$. Besides, it involves the inversion of a potentially high-dimensional covariance matrix $\Sigma_{\mathbf{Z}}$, which makes direct calculation or any operation on Φ difficult, if not completely infeasible. Next, we consider a dimension reduction model for Φ , which reduces the dimensionality, avoids $\Sigma_{\mathbf{Z}}^{-1}$, and improves the interpretability of the results. We also discuss the normality assumption in more detail, and show that it is *not* absolutely necessary.

2.2 Dimension reduction model for generalized liquid association analysis

Our key idea of dimension reduction is to look for linear combinations of \mathbf{X} and \mathbf{Y} that change the most as \mathbf{Z} or some of its linear combinations change. Moreover, we show that dropping $\Sigma_{\mathbf{Z}}^{-1}$

would not affect our search for such linear combinations of \mathbf{X} and \mathbf{Y} .

Specifically, we first postulate that the matrix $\mathbf{g}(\mathbf{z}) = \mathbb{E}(\mathbf{X}\mathbf{Y}^T | \mathbf{Z} = \mathbf{z}) \in \mathbb{R}^{p_1 \times p_2}$ varies within a low-dimensional subspace for all values of \mathbf{z} , in that

$$\mathbf{g}(\mathbf{z}) = \mathbb{E}(\mathbf{X}\mathbf{Y}^T | \mathbf{Z} = \mathbf{z}) = \mathbf{\Gamma}_1 \mathbf{f}(\mathbf{z}) \mathbf{\Gamma}_2^T,$$

for some semi-orthogonal basis matrices $\mathbf{\Gamma}_k \in \mathbb{R}^{p_k \times r_k}$, $k = 1, 2$, and some latent function $\mathbf{f} : \mathbb{R}^{r_3} \mapsto \mathbb{R}^{r_1 \times r_2}$. This implies that the linear combinations $\mathbf{\Gamma}_1^T \mathbf{X}$ and $\mathbf{\Gamma}_2^T \mathbf{Y}$ capture all the variations in the generalized liquid association measure. Next, we further assume that the generalized liquid association depends on \mathbf{Z} only through a few linear combinations $\mathbf{\Gamma}_3^T \mathbf{Z}$ of \mathbf{Z} , for some semi-orthogonal basis matrix $\mathbf{\Gamma}_3 \in \mathbb{R}^{p_3 \times r_3}$. Putting these two dimension reduction structures together, we obtain our dimension reduction model for the generalized liquid association analysis,

$$\mathbf{g}(\mathbf{z}) = \mathbb{E}(\mathbf{X}\mathbf{Y}^T | \mathbf{Z} = \mathbf{z}) = \mathbf{\Gamma}_1 \mathbf{f}(\mathbf{\Gamma}_3^T \mathbf{z}) \mathbf{\Gamma}_2^T, \quad (1)$$

Given this model, we have the following result.

Proposition 2. *Under model (1), if $\mathbf{\Gamma}_3^T \mathbf{Z}$ is normally distributed, then*

$$\mathbf{\Phi} = \mathbf{\Phi} \times_1 \mathbf{P}_{\mathbf{\Gamma}_1} \times_2 \mathbf{P}_{\mathbf{\Gamma}_2} \times_3 \mathbf{P}_{\mathbf{\Gamma}_3} = \mathbf{\Phi} \times_k \mathbf{P}_{\mathbf{\Gamma}_k},$$

where $\mathbf{P}_{\mathbf{\Gamma}_k} = \mathbf{\Gamma}_k (\mathbf{\Gamma}_k^T \mathbf{\Gamma}_k)^{-1} \mathbf{\Gamma}_k^T$ denotes the projection onto the subspace $\text{span}(\mathbf{\Gamma}_k)$ spanned by the columns of $\mathbf{\Gamma}_k$, and \times_k denotes the mode- k product between a tensor and a matrix, $k = 1, 2, 3$.

An important implication of this proposition is that it points a way to estimate the linear combination coefficients $\mathbf{\Gamma}_k$ that we seek in the dimension reduction model (1), or more accurately, the subspace $\text{span}(\mathbf{\Gamma}_k)$ spanned by the columns of $\mathbf{\Gamma}_k$, $k = 1, 2, 3$. That is, following Proposition 2, we can re-formulate $\mathbf{\Gamma}_k$'s as the solutions to the following optimization problem,

$$\text{minimize}_{\mathbf{G}_1, \mathbf{G}_2, \mathbf{G}_3} \|\mathbf{\Phi} - \mathbf{\Phi} \times_1 \mathbf{P}_{\mathbf{G}_1} \times_2 \mathbf{P}_{\mathbf{G}_2} \times_3 \mathbf{P}_{\mathbf{G}_3}\|_F^2, \quad (2)$$

where $\mathbf{G}_k \in \mathbb{R}^{p_k \times r_k}$, $k = 1, 2, 3$, are the semi-orthogonal matrices. The optimization in (2) is actually the well-known tensor Tucker decomposition (Kolda and Bader, 2009).

Moreover, let $(\tilde{\mathbf{G}}_1, \tilde{\mathbf{G}}_2, \tilde{\mathbf{G}}_3)$ denote the minimizer of (2). Then $(\tilde{\mathbf{G}}_1, \tilde{\mathbf{G}}_2, \tilde{\mathbf{G}}_3)$ is the solution to the maximization problem,

$$\text{maximize}_{\mathbf{G}_1, \mathbf{G}_2, \mathbf{G}_3} \|\mathbf{\Phi} \times_1 \mathbf{P}_{\mathbf{G}_1} \times_2 \mathbf{P}_{\mathbf{G}_2} \times_3 \mathbf{P}_{\mathbf{G}_3}\|_F^2.$$

In other words, solving (2) helps find the linear combinations of \mathbf{X} and \mathbf{Y} whose generalized liquid association given some linear combination of \mathbf{Z} is maximized under model (1). In this sense, it achieves our goal of finding the most contrastive associations of \mathbf{X} and \mathbf{Y} given \mathbf{Z} .

An issue with (2), however, is the computation of the generalized liquid association measure Φ still involves the matrix $\Sigma_{\mathbf{Z}}^{-1}$. Next, we show that we can essentially drop $\Sigma_{\mathbf{Z}}^{-1}$ in our generalized liquid association analysis. Toward that end, we define $\Delta = \mathbb{E}(\mathbf{X} \circ \mathbf{Y} \circ \mathbf{Z}) \in \mathbb{R}^{p_1 \times p_2 \times p_3}$. By Proposition 1, $\Phi = \Delta \times_3 \Sigma_{\mathbf{Z}}^{-1}$. We then consider the following optimization problem,

$$\text{minimize}_{\mathbf{G}_1, \mathbf{G}_2, \mathbf{G}_3} \|\Delta - \Delta \times_1 \mathbf{P}_{\mathbf{G}_1} \times_2 \mathbf{P}_{\mathbf{G}_2} \times_3 \mathbf{P}_{\mathbf{G}_3}\|_F^2, \quad (3)$$

where $\mathbf{G}_k \in \mathbb{R}^{p_k \times r_k}$, $k = 1, 2, 3$, are the semi-orthogonal matrices. The optimization in (3) is still a Tucker decomposition problem. However, it is much easier to compute Δ given the data, as it involves no matrix inversion. Let $(\hat{\mathbf{G}}_1, \hat{\mathbf{G}}_2, \hat{\mathbf{G}}_3)$ denote the minimizer of (3). The next proposition connects the minimization problem (3) with (2).

Proposition 3. *Under model (1), $\text{span}(\Gamma_k) = \text{span}(\tilde{\mathbf{G}}_k) = \text{span}(\hat{\mathbf{G}}_k)$, $k = 1, 2$. If $\Gamma_3^T \mathbf{Z}$ is normally distributed, then $\text{span}(\Gamma_3) = \text{span}(\tilde{\mathbf{G}}_3) = \Sigma_{\mathbf{Z}}^{-1} \text{span}(\hat{\mathbf{G}}_3)$.*

A few remarks are in order. First of all, Proposition 3 suggests that minimizing (3) gives the same estimates of Γ_1 and Γ_2 in model (1) as minimizing (2), in the sense that they span the same subspaces. Meanwhile, the estimates of Γ_3 under the two minimization problems differ by a rotation. In the generalized liquid association analysis, our primary goal is to find linear combinations of \mathbf{X} and \mathbf{Y} that are the most contrastive given \mathbf{Z} . As such, we are more interested in the estimation of Γ_1 and Γ_2 , whereas the estimation of Γ_3 provides additional dimension reduction, but is, relatively speaking, of less interest. This justifies to focus on the minimization problem (3) instead of (2) in our generalized liquid association analysis.

Second, we discuss more about the normality assumption. The normality of \mathbf{Z} allows us to use Stein's Lemma to link the generalized liquid association measure Φ with the expectation tensor Δ , as shown in Proposition 1. This assumption is commonly imposed in the liquid association analysis literature, and is often achieved by normal score transformation of data (Li, 2002; Li et al., 2004; Yu, 2018). On the other hand, we argue this assumption is *not* that crucial for our proposed generalized liquid association analysis. This is because, as shown in Proposition 3, the estimation of Γ_1 and Γ_2 does not really require the normality assumption. When it holds, we are

able to connect the minimizer of (3) with the generalized liquid association measure. When it does not hold, we lose this interpretation. Instead, we seek the linear combinations in the dimension reduction model (1) that target the function $\mathbf{g}(\mathbf{z})$, rather than the expectation of the derivative of $\mathbf{g}(\mathbf{z})$. In other words, the minimization problem in (3) is still meaningful and provides useful information, but admits a different interpretation. Actually, this is similar in spirit to one of the sufficient dimension reduction methods, the principal Hessian directions (Li, 1992). It was also derived based on Stein’s Lemma, but was shown to be useful for finding low-dimensional representations in graphics (Cook, 1998), and for detecting interaction terms in regressions (Tang et al., 2020), even without the normality assumption.

3 Sparse Tensor Estimation

Tucker decomposition is usually solved by a higher-order singular value decomposition (HOSVD) algorithm or its variants. Next, we develop an iterative HOSVD algorithm to solve (3). We further introduce sparsity in this decomposition to improve the interpretability of the results.

For n i.i.d. data observations $\{\mathbf{X}_i, \mathbf{Y}_i, \mathbf{Z}_i, i = 1, \dots, n\}$, without loss of generality, we assume the data is centered, so that $\sum_{i=1}^n \mathbf{Z}_i = 0$. The centering of \mathbf{X} and \mathbf{Y} is not required, but for simplicity, we assume $\sum_{i=1}^n \mathbf{X}_i = \sum_{i=1}^n \mathbf{Y}_i = 0$ as well. Then the sample estimator of $\mathbf{\Delta}$ is simply $\tilde{\mathbf{\Delta}} = n^{-1} \sum_{i=1}^n \mathbf{X}_i \circ \mathbf{Y}_i \circ \mathbf{Z}_i \in \mathbb{R}^{p_1 \times p_2 \times p_3}$. Following the dimension reduction model (1) and the optimization problem (3), $\tilde{\mathbf{\Delta}}$ admits a Tucker tensor decomposition structure, which can be solved by some version of the higher-order singular value decomposition algorithm. Specifically, we simplify the STAT-SVD algorithm recently proposed by Zhang and Han (2019) for the tensor denoising problem, and tailor it to our generalized liquid association analysis problem to estimate $\mathbf{\Gamma}_k, k = 1, 2, 3$. It consists of two major components, SVD of a matrix, and hard thresholding to identify important variables. We summarize the estimation procedure in Algorithm 1, then discuss each step in detail. We also note that, in our formulation, we allow the number of variables $p_k, k = 1, 2, 3$, to be much larger than the sample size n .

We first introduce some notation. For an integer p , let $[p]$ denote the set $\{1, \dots, p\}$. For a matrix $\mathbf{A} \in \mathbb{R}^{p \times q}$ and index sets $I \subseteq [p], J \subseteq [q]$, let $\mathbf{A}_{[I, J]}$ denote the corresponding $|I| \times |J|$ submatrix, while the whole index set $[p]$ is simplified as “.”; e.g., $\mathbf{A}_{[[p], J]} = \mathbf{A}_{[., J]}$. Let $\tilde{\mathbf{\Delta}}_k$ and $\mathbf{\Delta}_k$ denote the mode- k matricization of the tensors $\mathbf{\Delta}$ and $\tilde{\mathbf{\Delta}}, k = 1, 2, 3$. Define $\mathbf{\Gamma}_{-1} =$

Algorithm 1 Generalized liquid association analysis via sparse tensor decomposition.

Input: The Tucker ranks $r_k \leq p_k$, and the sparsity parameters $(\eta_k, \tilde{\eta}_k)$, $k = 1, 2, 3$.

Step 1, initialization: Compute the sample estimate $\tilde{\Delta} = n^{-1} \sum_{i=1}^n \mathbf{X}_i \circ \mathbf{Y}_i \circ \mathbf{Z}_i$. Obtain the initial active set $\hat{I}_k^{(0)}$, and the initial basis matrices by,

$$\hat{I}_k^{(0)} = \left\{ j : \|(\tilde{\Delta}_k)_{[j,:]} \|_{\max} > \eta_k \right\}, \quad \hat{\Gamma}_k^{(0)} = \text{SVD} \left\{ \mathbf{D}_{\hat{I}_k^{(0)}} \tilde{\Delta}_k \mathbf{D}_{\hat{I}_{-k}^{(0)}} \right\}, \quad k = 1, 2, 3.$$

repeat

Step 2a: Update the active set: $\hat{I}_k^{(t)} = \left\{ j : \|(\tilde{\Delta}_k)_{[j,:]} \hat{\Gamma}_{-k}^{(t)} \|_2^2 > \tilde{\eta}_k \right\}$, $k = 1, 2, 3$.

Step 2b: Perform SVD: $\hat{\Gamma}_k^{(t)} = \text{SVD} \left\{ \mathbf{D}_{\hat{I}_k^{(t)}} \tilde{\Delta}_k \hat{\Gamma}_{-k}^{(t)} \right\} \in \mathbb{R}^{p_k \times r_k}$, $k = 1, 2, 3$.

until the stopping criterion is met.

Output: The estimated basis matrices $\hat{\Gamma}_k$, $k = 1, 2, 3$, and $\hat{\Delta} = \tilde{\Delta} \times_1 \mathbf{P}_{\hat{\Gamma}_1} \times_2 \mathbf{P}_{\hat{\Gamma}_2} \times_3 \mathbf{P}_{\hat{\Gamma}_3}$.

$\Gamma_2 \otimes \Gamma_3, \Gamma_{-2} = \Gamma_3 \otimes \Gamma_1, \Gamma_{-3} = \Gamma_1 \otimes \Gamma_2$, where \otimes is the Kronecker product. Next, we define the active sets of variables in the context of generalized liquid association analysis as,

$$I_k = \left\{ j : (\Delta_k)_{[j,:]} \neq 0, 1 \leq j \leq p_k \right\} \subseteq [p_k], \quad k = 1, 2, 3. \quad (4)$$

As an example, the j th variable X_j in \mathbf{X} corresponds to the j th row of $\Gamma_1 \in \mathbb{R}^{p_1 \times r_1}$, $j = 1, \dots, p_1$. Therefore, variable selection in \mathbf{X} translates to the row-wise sparsity in Γ_1 , and correspondingly, the row-wise sparsity in $\Delta_1 \in \mathbb{R}^{p_1 \times p_2 p_3}$. Define the diagonal matrix $\mathbf{D}_{I_k} \in \mathbb{R}^{p_k \times p_k}$ that has one on the i th diagonal element if $i \in I_k$ and zero elsewhere. This matrix represents variable selection along each mode, and is used repeatedly in our estimation algorithm. Define $\mathbf{D}_{I_{-1}} = \mathbf{D}_{I_2} \otimes \mathbf{D}_{I_3}$, whereas I_{-1} denotes the pair of subsets I_2 and I_3 . Define $\mathbf{D}_{I_{-2}}, \mathbf{D}_{I_{-3}}, I_{-2}, I_{-3}$ similarly. Also define $\hat{\Gamma}_{-k}, \hat{I}_k$, $k = 1, 2, 3$, in a similar fashion.

We start the algorithm by computing the sample estimate $\tilde{\Delta}$, then perform the initial selection of important variables and initial SVD in Step 1 of Algorithm 1. From (4), we see that the selection of important variables can be achieved based on $\|(\Delta_k)_{[j,:]} \|$ for some appropriate norm $\| \cdot \|$. In the initialization step, we employ the maximum norm, and achieve the selection by hard thresholding under the sparsity parameter η_k . The two diagonal matrices $\mathbf{D}_{\hat{I}_k^{(0)}}$ and $\mathbf{D}_{\hat{I}_{-k}^{(0)}}$ operate as the subset selection operator within the SVD operator. Moreover, depending on the sparsity parameter η_k , we may keep all the variables in the active set, i.e., $\hat{I}_k = [p_k]$.

Next, we iterate the algorithm by repeatedly selecting important variables and performing SVD in Step 2 of Algorithm 1. We continue to do the selection by hard thresholding, but we use

a different norm, i.e., the ℓ_2 -norm rather than the max-norm, and a different sparsity parameter $\tilde{\eta}_k$. This change of the norm is practically useful because of the following consideration. In the initialization step, the column dimension of $\tilde{\Delta}_k$ is $\prod_{k' \neq k} p_{k'}$ and is often very large, and thus the maximum norm is more effective in screening out the zero rows in $\tilde{\Delta}_k$. On the other hand, during the iterations, the active variable set I_k is selected based on $\tilde{\Delta}_k \Gamma_{-k}$, which now has a much smaller column dimension, which is $\prod_{k' \neq k} r_{k'}$. As such, the ℓ_2 -norm is preferred to being able to pick up potentially weaker signals and to refine the selection from the initialization. Moreover, a different thresholding parameter $\tilde{\eta}_k$ during the iterations gives more flexibility.

We alternate Steps 2a and 2b until some termination criterion is met. That is, we terminate the algorithm if the consecutive estimates are close enough, in that the difference between the ℓ_2 -norm of the singular values of the two iterations is smaller than 10^{-6} , or the algorithm reaches the maximum number of iterations pre-specified at 100. In our numerical experiments, we find that the algorithm converges fast, usually within 10 to 20 iterations. We output the estimated basis matrices $\hat{\Gamma}_k$, $k = 1, 2, 3$, along with the updated estimate $\hat{\Delta} = \tilde{\Delta} \times_1 P_{\hat{\Gamma}_1} \times_2 P_{\hat{\Gamma}_2} \times_3 P_{\hat{\Gamma}_3}$ that follows a Tucker decomposition.

Our algorithm is related to the STAT-SVD algorithm of Zhang and Han (2019), in that we all use hard thresholding SVD iteratively. On the other hand, Zhang and Han (2019) targeted a tensor denoising problem involving identically distributed normal errors, and used a double thresholding scheme with a theoretical thresholding value. Their algorithm, after obtaining the variance of the errors, became tuning-free in terms of the thresholding parameter. By contrast, we aim to obtain a low-rank tensor estimator in the context of generalized liquid association analysis. The sample estimator does not have i.i.d. entries, and we use a single thresholding scheme with two data-driven tuning parameters. This leads to a more flexible tuning, and consequently an utterly different approach for the asymptotic analysis.

The thresholding values η_k and $\tilde{\eta}_k$ are treated as tuning parameters, and we propose a prediction-based approach for tuning. That is, we first randomly split the data into a training set and a testing set, and obtain the sample estimates $\tilde{\Delta}^{\text{train}}$ and $\tilde{\Delta}^{\text{test}}$ separately. We then apply Algorithm 1 to $\tilde{\Delta}^{\text{train}}$ to obtain $\hat{\Gamma}_k^{\text{train}}(\eta)$, $k = 1, 2, 3$, under a given set of tuning parameters $\eta = (\eta_1, \eta_2, \eta_3, \tilde{\eta}_1, \tilde{\eta}_2, \tilde{\eta}_3)$. We choose η such that the following discrepancy is minimized,

$$L(\eta) = \left\| \tilde{\Delta}^{\text{test}} - \tilde{\Delta}^{\text{test}} \times_1 P_{\hat{\Gamma}_1^{\text{train}}(\eta)} \times_2 P_{\hat{\Gamma}_2^{\text{train}}(\eta)} \times_3 P_{\hat{\Gamma}_3^{\text{train}}(\eta)} \right\|_F. \quad (5)$$

Meanwhile, the ranks (r_1, r_2, r_3) take some pre-specified values. In practice, r_k is often taken as 1 or 2 for exploratory analysis and data visualization. This is the same in spirit as canonical correlation analysis. Actually, rank selection is still an open question in both CCA and matrix or tensor denoising, and we leave a full treatment of rank selection as future research.

4 Theoretical Properties

We establish the theoretical guarantees for the estimated subspace basis matrices $\widehat{\Gamma}_k$, the estimated Tucker tensor $\widehat{\Delta} = \widetilde{\Delta} \times_1 \mathbf{P}_{\widehat{\Gamma}_1} \times_2 \mathbf{P}_{\widehat{\Gamma}_2} \times_3 \mathbf{P}_{\widehat{\Gamma}_3}$, and the estimated active sets $\widehat{I}_k^{(t)}$, $k = 1, 2, 3$, from Algorithm 1. We first lay out the required regularity conditions, then derive the non-asymptotic error bounds and the asymptotic consistency. In our theoretical analysis, we allow both the tensor dimension $p = \prod_{k=1}^3 p_k$ and the sparsity level $s = \prod_{k=1}^3 s_k$ to diverge with the sample size n , while we fix the tensor rank $r = \prod_{k=1}^3 r_k$. Throughout this section, we use C and C' to denote some generic positive constants that could vary in different contexts.

We begin with three technical assumptions.

- (A1) (Marginal distribution). Assume $|X_i Y_j| \leq C$ for some constant $C > 0$, $i = 1, \dots, p_1, j = 1, \dots, p_2$. Assume Z_k is sub-Gaussian with a constant parameter $\sigma^2 > 0$, $k = 1, \dots, p_3$.
- (A2) (Singular value). Let λ_k denote the smallest non-zero singular value of Δ_k , $k = 1, 2, 3$, and $\lambda = \min\{\lambda_1, \lambda_2, \lambda_3\}$. Assume $\lambda > \max\{C\sqrt{s \log p/n}, C'\}$ for some constants $C, C' > 0$.
- (A3) (Signal strength). Let $\delta_{\min} = \min_{k \in \{1, 2, 3\}, i \in I_k} \|(\Delta_k)_{[i, \cdot]}\|_2$ denote the minimal signal strength. Assume $\sqrt{s \log p/n} = o(\delta_{\min})$.

We view these assumptions generally mild and reasonable. Particularly, Assumption (A1) requires \mathbf{X} and \mathbf{Y} to be bounded and \mathbf{Z} to be sub-Gaussian, which are necessary to establish the concentration of each element in $\widetilde{\Delta}$ to its population counterpart. The sub-Gaussian assumption is weaker than the normality assumption, and is widely used in high-dimensional non-asymptotic analysis (see, e.g., Rudelson and Vershynin, 2010; Wainwright, 2019). Besides, it assumes each individual Z_k to be sub-Gaussian, which is weaker than assuming the joint distribution \mathbf{Z} is sub-Gaussian. Moreover, the constant $\sigma^2 > 0$ does not require all Z_k to have the same variance. For instance, if Z_k is sub-Gaussian with parameter σ_k^2 , $k = 1, \dots, p_3$, then we can let $\sigma^2 = \max_k \sigma_k^2$

to have Assumption (A1) satisfied. Assumption (A2) ensures that there is a reasonable gap between the zero and nonzero eigenvalues in Δ_k , under which the consistency for the estimator $\widehat{\Gamma}_k$ is ensured. This type of assumption on the eigenvalues is frequently used in high-dimensional singular value decomposition literature (Yu et al., 2015; Yang et al., 2016; Zhang and Han, 2019). Assumption (A3) guarantees that the signal of the important variables is of a reasonable magnitude when n, p, s diverge, which in turn ensures the selection consistency. Note that δ_{\min} is also the minimal Frobenius norm of the non-zero slices in Δ , i.e., slices of Δ corresponding to those variables $i \in I_k, k = 1, 2, 3$. This assumption is very mild. If we assume the nonzero entries of Δ are bounded away from zero, then this assumption is satisfied.

Next, we derive the non-asymptotic error bounds of the generalized liquid association analysis estimators. Let $\widehat{\Delta}$ and $\widehat{\Gamma}_k, k = 1, 2, 3$, denote the estimators returned from Algorithm 1, using the theoretical thresholding values $\eta_k = \sqrt{\alpha \log p/n}$ and $\tilde{\eta}_k = \alpha s_{-k} \log p/n$, where $\alpha > 512(C + \sigma)^4$ is a sufficiently large constant, and C, σ are as defined in Assumption (A1). Moreover, since the basis matrix $\widehat{\Gamma}_k$ is identifiable only up to an orthogonal rotation, we characterize its convergence in terms of the corresponding projection matrix $\mathbf{P}_{\widehat{\Gamma}_k}, k = 1, 2, 3$.

Theorem 1 (Non-asymptotic error bound). *Suppose Assumptions (A1) and (A2) hold. Then, with probability at least $1 - C \max \left[p^{-\gamma}, p^{-\left\{ \sqrt{n(\gamma+1)/(2 \log p)} - 1 \right\}} \right]$, for some constant $\gamma > 0$,*

$$(a) \quad \|\widehat{\Delta} - \Delta\|_F \leq C \sqrt{s \log p/n};$$

$$(b) \quad \max_{k=1,2,3} \|\mathbf{P}_{\widehat{\Gamma}_k} - \mathbf{P}_{\Gamma_k}\|_F \leq C \sqrt{s \log p/n}.$$

When the sample size is sufficiently large, i.e., when $n \gg 2(\gamma + 1) \log p$, both statements in Theorem 1 hold with probability $1 - Cp^{-\gamma}$. This probability goes to one as p diverges with n . We also briefly comment that, although we establish Theorem 1 for an order-3 tensor, the results can be straightforwardly extended for a general order tensor.

Next, we establish the asymptotic consistency as n, p, s diverge to infinity.

Theorem 2 (Asymptotic consistency). *Suppose Assumptions (A1) to (A3) hold. Then, with probability tending to one, as $n, p, s \rightarrow \infty$, we have,*

$$(a) \quad \|\widehat{\Delta} - \Delta\|_F \rightarrow 0;$$

$$(b) \quad \|\mathbf{P}_{\widehat{\Gamma}_k} - \mathbf{P}_{\Gamma_k}\|_F \rightarrow 0, k = 1, 2, 3;$$

(c) $\widehat{I}_k^{(t)} = I_k$, $k = 1, 2, 3$, and for iterations $t = 0, 1, \dots, t_{\max}$.

Theorem 2 establishes the consistency of tensor parameter estimation, subspace estimation, as well as variable selection, under $s \log p = o(n)$, which allows each tensor dimension p_k to diverge faster than the growing sample size n . Moreover, the consistent variable selection is established for every iteration of Algorithm 1. Note that the maximum number of iterations t_{\max} in Theorem 2 (c) is treated as a constant regardless of the tensor dimension or sample size. In practice, we have observed that the algorithm often converges within 10 to 20 iterations. As such, we feel it reasonable to treat t_{\max} as a constant in our theoretical analysis. On the other hand, we can extend the result by allowing t_{\max} to diverge as well. For instance, parallel to the arguments in Zhang and Han (2019), we can let t_{\max} diverge at the rate of $o(p)$.

Theorems 1 and 2 provide the theoretical guarantees for our proposed generalized liquid association analysis in the high dimensional setting. At the same time, these results may be of independent interest for more general tensor estimation problems.

5 Simulation Studies

5.1 Simulation setup

We carry out the simulations to investigate the empirical performance of the proposed generalized liquid association analysis (GLAA) method. We consider three scenarios. In the first scenario, we fix the dimension of \mathbf{Z} at $p_3 = 1$, and increase the dimensions of \mathbf{X} and \mathbf{Y} as $p_1 = p_2 = \{100, 200, 300, 400, 500\}$. In the second scenario, we fix $p_1 = p_2 = 100$, and increase $p_3 = \{20, 40, 60, 80, 100\}$. In both cases, we fix the sample size at $n = 500$. In the third scenario, we fix $p_1 = 100, p_2 = 25, p_3 = 1$, and increase the sample size $n = \{60, 80, 100, 120, 160\}$.

We generate the data in the following way. For $i = 1, \dots, n$, we first generate \mathbf{Z}_i from a normal distribution with mean zero and covariance \mathbf{I}_{p_3} . We then generate $(\mathbf{X}_i, \mathbf{Y}_i)$ jointly from a normal distribution with mean zero and covariance,

$$\text{cov}(\mathbf{X}, \mathbf{Y} \mid \mathbf{Z} = \mathbf{Z}_i) = \begin{pmatrix} \Sigma_{\mathbf{X}} & \Gamma_1 \mathbf{f}(\Gamma_3^\top \mathbf{Z}_i) \Gamma_2^\top \\ \Gamma_2 \mathbf{f}^\top(\Gamma_3^\top \mathbf{Z}_i) \Gamma_1^\top & \Sigma_{\mathbf{Y}} \end{pmatrix}.$$

To ensure the positive-definiteness of this covariance matrix, we set $\Gamma_1 = \Sigma_{\mathbf{X}}^{1/2}(\mathbf{O}_1^\top, \mathbf{0})^\top$ and $\Gamma_2 = \Sigma_{\mathbf{Y}}^{1/2}(\mathbf{O}_2^\top, \mathbf{0})^\top$, where $\mathbf{O}_1 = \mathbf{O}_2 \in \mathbb{R}^{5 \times 2}$, with the first column being $(1, 1, 1, 1, 1, 0, \dots, 0)^\top$.

$\sqrt{5}$, and the second column being $(0, 0, 0, -1, 1, 0, \dots, 0)/\sqrt{2}$. As a result, in this example, for \mathbf{X} and \mathbf{Y} , the ranks are $r_1 = r_2 = 2$, and the sparsity levels are $s_1 = s_2 = 5$. The marginal covariance matrix $\Sigma_{\mathbf{X}}$ is set as a block diagonal matrix, $\Sigma_{\mathbf{X}} = \text{bdiag}(\Sigma_{\mathbf{X},1}, \Sigma_{\mathbf{X},2})$, where $\Sigma_{\mathbf{X},1} \in \mathbb{R}^{s_1 \times s_1}$ corresponds to the active variables in \mathbf{X} and takes the form of an AR structure such that its (i, j) th entry equals $\sigma_{ij} = 0.3^{|i-j|}$, $i, j = 1, \dots, s_1$, and $\Sigma_{\mathbf{X},2} \in \mathbb{R}^{(p_1-s_1) \times (p_1-s_1)}$ is the identity matrix. The marginal covariance matrix $\Sigma_{\mathbf{Y}}$ is constructed in a similar fashion. The matrix $\mathbf{f}(\Gamma_3^\top \mathbf{Z}_i)$ is set as a diagonal matrix, $\text{diag}\{f_1(\Gamma_3^\top \mathbf{Z}_i), f_2(\Gamma_3^\top \mathbf{Z}_i)\}$, where $f_1(a) = 0.95\text{sign}(a)$ and $f_2(a) = 0.85\text{sign}(a)$. In the Supplementary Appendix, we consider additional simulations using $f(a; \rho, \xi) = \rho\{2/(1 + e^{-2\xi a}) - 1\}$ with different parameters $0 < \rho \leq 1$ and $\xi > 0$ that control the magnitude and speed of changes in $\text{cov}(\mathbf{X}, \mathbf{Y} | \mathbf{Z})$. For the first and the third scenarios, $p_3 = 1$ and thus $\Gamma_3 = 1$. For the second scenario, where p_3 varies from 20 to 100, we set $\Gamma_3 = (1, 1, 1, 1, 1, 0, \dots, 0)/\sqrt{5}$, with $s_3 = 5$.

When applying the proposed method, we choose η_1 and η_2 , which are the thresholding parameters only used in the initialization step of the algorithm, so that about half of the variables in \mathbf{X} and in \mathbf{Y} are kept for subsequent iterations. We then tune $\tilde{\eta}_1$ and $\tilde{\eta}_2$, the thresholding parameters used in iterative sparse SVD, by cross-validation over a grid of candidate values. We choose the ranks r_1, r_2 , i.e., the numbers of linear combinations for \mathbf{X} and \mathbf{Y} , to be one, which is most commonly used in canonical correlation analysis as well.

There is no existing method designed to directly address our targeting problem. For the purpose of comparison, we consider three relevant solutions. The first solution we consider is a naive and marginal extension of the univariate liquid association (ULA) method from Li (2002). That is, we construct a tensor estimator $\tilde{\Phi}$, each entry of which is the sample univariate LA for the triplet $(X_{i_1}, Y_{i_2}, Z_{i_3})$ as defined in Li (2002), $i_1 = 1, \dots, p_1, i_2 = 1, \dots, p_2, i_3 = 1, \dots, p_3$. We then perform the usual HOSVD to each matricization of $\tilde{\Phi}$ under the given rank to obtain the estimates of basis matrices; i.e., $\text{SVD}\{\tilde{\Phi}_{(k)}\}$, $k = 1, 2, 3$. The second and third solutions we consider are two different versions of canonical correlation analysis, the penalized matrix decomposition (PMD) method of Witten et al. (2009), and the sparse canonical correlation analysis (SCCA) method of Mai and Zhang (2019). We have chosen these two versions due to their computational simplicity and superior empirical performance. We note that CCA is not designed to incorporate the third set of variables \mathbf{Z} . We thus simply take the first r_1 and r_2 directions of \mathbf{X} and \mathbf{Y} from CCA as the estimated basis matrices corresponding to Γ_1 and Γ_2 .

We evaluate the performance of each method in terms of the variable selection accuracy and the subspace estimation accuracy.

For variable selection, we record the true positive rate (TPR) and false positive rate (FPR) for each mode. Recall from (4), the active set of variables is I_k , which is also the index set of nonzero rows in Γ_k . Let \hat{I}_k denote the estimated active set corresponding to $\hat{\Gamma}_k$, then $\text{TPR-}k = |I_k \cap \hat{I}_k|/s_k$ and $\text{FPR-}k = |I_k^c \cap \hat{I}_k|/(p_k - s_k)$, $k = 1, 2, 3$. For GLAA, PMD and SCCA, we estimate the active set as $\hat{I}_k = \left\{ i : \text{there exist non-zero elements in the } i\text{th row of } \hat{\Gamma}_k \right\}$. For ULA, it does not perform any variable selection. For the purpose of comparison, we simply calculate the ℓ_2 -norm of each row for the k th matricization $\tilde{\Phi}_{(k)}$, arrange the row indices in a descending order by the ℓ_2 -norms, then select the first s_k rows for each mode, $k = 1, 2, 3$. Of course, the information about s_k is generally unknown in practice, and this solution utilizes such knowledge. Even so, as we show later, ULA is still far less effective compared to the proposed GLAA method.

For subspace estimation, we compute the average distance between the true and the estimated subspaces, $D = \sum_{k=1}^{\tilde{k}} D(\Gamma_k, \hat{\Gamma}_k)/\tilde{k}$, where $D(\Gamma_k, \hat{\Gamma}_k) = \|\mathbf{P}_{\Gamma_k} - \mathbf{P}_{\hat{\Gamma}_k}\|_F/\sqrt{2r_k}$. For GLAA and ULA, this distance measure is averaged over all three modes of $\mathbf{X}, \mathbf{Y}, \mathbf{Z}$, so $\tilde{k} = 3$. For PMD and SCCA, it is averaged over the first two modes \mathbf{X}, \mathbf{Y} , so $\tilde{k} = 2$. By definition, this distance measure is between 0 and 1, where 0 indicates a perfect subspace recovery.

5.2 Simulation results

Tables 1–3 summarize the simulation results over 100 data replications for the three scenarios.

Table 1 reports the accuracy of variable selection and subspace estimation when the dimension $p_1 = p_2$ of \mathbf{X} and \mathbf{Y} increases. It is clearly seen that GLAA dominates all the competing solutions. For ULA, variable selection and subspace estimation are carried out separately. Even with the oracle knowledge of the true sparsity level, the naive variable selection of ULA still performs worse, as it only utilizes the marginal information of each mode. Besides, the estimated subspace is distant away from the true subspace, especially when p_1, p_2 are large. Moreover, we see that, as p_1, p_2 increase, the performance of ULA degrades fast, while GLAA remains competitive. For PMD and SCCA, both suffer large false positive rates in selection, while the estimated subspaces are almost orthogonal to the true subspace, as reflected by the distance measure D that is almost one. This is due to the fact that, by design, neither method takes into account the conditioning variable \mathbf{Z} information when studying the association between \mathbf{X} and \mathbf{Y} .

p_1, p_2	Method	TPR-1	FPR-1	TPR-2	FPR-2	D
100	GLAA	1.000 (0.000)	0.000 (0.000)	1.000 (0.000)	0.000 (0.000)	0.095 (0.002)
	ULA	0.998 (0.002)	0.000 (0.000)	0.996 (0.003)	0.000 (0.000)	0.776 (0.002)
	PMD	0.804 (0.028)	0.735 (0.029)	0.802 (0.029)	0.731 (0.028)	0.971 (0.002)
	SCCA	0.584 (0.030)	0.626 (0.027)	0.634 (0.030)	0.629 (0.027)	0.989 (0.001)
200	GLAA	1.000 (0.000)	0.000 (0.000)	1.000 (0.000)	0.000 (0.000)	0.100 (0.003)
	ULA	0.928 (0.010)	0.002 (0.000)	0.944 (0.009)	0.001 (0.000)	0.873 (0.002)
	PMD	0.766 (0.033)	0.731 (0.029)	0.762 (0.033)	0.727 (0.029)	0.989 (0.001)
	SCCA	0.596 (0.031)	0.611 (0.027)	0.626 (0.035)	0.611 (0.027)	0.993 (0.001)
300	GLAA	1.000 (0.000)	0.000 (0.000)	1.000 (0.000)	0.000 (0.000)	0.100 (0.003)
	ULA	0.808 (0.016)	0.003 (0.000)	0.806 (0.016)	0.003 (0.000)	0.945 (0.003)
	PMD	0.718 (0.032)	0.693 (0.030)	0.730 (0.034)	0.696 (0.029)	0.992 (0.001)
	SCCA	0.670 (0.028)	0.651 (0.019)	0.624 (0.028)	0.651 (0.018)	0.997 (0.000)
400	GLAA	0.932 (0.024)	0.008 (0.004)	0.930 (0.025)	0.008 (0.004)	0.186 (0.025)
	ULA	0.652 (0.018)	0.004 (0.000)	0.678 (0.019)	0.004 (0.000)	0.980 (0.002)
	PMD	0.798 (0.029)	0.766 (0.026)	0.800 (0.029)	0.762 (0.026)	0.994 (0.001)
	SCCA	0.594 (0.022)	0.601 (0.010)	0.590 (0.024)	0.602 (0.010)	0.997 (0.000)
500	GLAA	0.848 (0.032)	0.041 (0.010)	0.848 (0.033)	0.040 (0.009)	0.304 (0.037)
	ULA	0.526 (0.021)	0.005 (0.000)	0.526 (0.020)	0.005 (0.000)	0.989 (0.001)
	PMD	0.788 (0.031)	0.727 (0.027)	0.794 (0.030)	0.729 (0.028)	0.995 (0.001)
	SCCA	0.532 (0.024)	0.518 (0.008)	0.532 (0.024)	0.516 (0.008)	0.997 (0.000)

Table 1: Variable selection accuracy, measured by TPR and FPR, and the subspace estimation accuracy, measured by D , for Scenario 1 where $p_1 = p_2$ varies. The reported are the average criteria, with the standard errors in the parenthesis, over 100 data replications.

Table 2 reports the variable selection and subspace estimation accuracy when the dimension p_3 of \mathbf{Z} increases. In this case, our goal is to estimate the subspaces spanned by $\Gamma_1, \Gamma_2, \Gamma_3$ accurately, meanwhile select the variables in \mathbf{X} and \mathbf{Y} accurately. It is seen that GLAA again outperforms all other methods considerably. Besides, it shows a competitive performance of GLAA even with a relatively large dimensionality of \mathbf{Z} . This also complements our real data example where the dimension of \mathbf{Z} is one.

Table 3 reports the variable selection and subspace estimation accuracy when the sample size n increases. The size of n we examine is comparable to that in our multimodal PET example. It is seen that GLAA performs the best, even under a relatively small sample size. Moreover, the performances of all methods improve as n increases. However, ULA suffers a poor subspace estimation accuracy, while both PMD and SCCA continue to suffer both high false positive rates and poor subspace estimation accuracy, even for a relatively large sample size.

p_3	Method	TPR-1	FPR-1	TPR-2	FPR-2	D
20	GLAA	1.000 (0.000)	0.000 (0.000)	1.000 (0.000)	0.000 (0.000)	0.132 (0.004)
	ULA	0.642 (0.019)	0.019 (0.001)	0.638 (0.019)	0.019 (0.001)	0.872 (0.003)
	PMD	0.774 (0.031)	0.733 (0.029)	0.776 (0.031)	0.732 (0.029)	0.978 (0.002)
	SCCA	0.518 (0.034)	0.534 (0.029)	0.536 (0.032)	0.532 (0.030)	0.989 (0.001)
40	GLAA	1.000 (0.000)	0.000 (0.000)	1.000 (0.000)	0.000 (0.000)	0.131 (0.004)
	ULA	0.488 (0.020)	0.027 (0.001)	0.498 (0.020)	0.026 (0.001)	0.888 (0.002)
	PMD	0.774 (0.031)	0.695 (0.030)	0.772 (0.032)	0.695 (0.029)	0.973 (0.002)
	SCCA	0.590 (0.034)	0.596 (0.031)	0.624 (0.033)	0.589 (0.031)	0.987 (0.001)
60	GLAA	1.000 (0.000)	0.000 (0.000)	1.000 (0.000)	0.000 (0.000)	0.136 (0.004)
	ULA	0.384 (0.020)	0.032 (0.001)	0.404 (0.020)	0.031 (0.001)	0.898 (0.002)
	PMD	0.748 (0.030)	0.694 (0.030)	0.754 (0.033)	0.701 (0.030)	0.973 (0.002)
	SCCA	0.564 (0.031)	0.537 (0.029)	0.572 (0.031)	0.541 (0.029)	0.985 (0.002)
80	GLAA	0.998 (0.002)	0.000 (0.000)	0.998 (0.002)	0.000 (0.000)	0.145 (0.005)
	ULA	0.378 (0.021)	0.033 (0.001)	0.368 (0.019)	0.033 (0.001)	0.903 (0.001)
	PMD	0.706 (0.033)	0.689 (0.031)	0.760 (0.032)	0.688 (0.031)	0.975 (0.002)
	SCCA	0.624 (0.031)	0.613 (0.027)	0.592 (0.033)	0.609 (0.027)	0.987 (0.002)
100	GLAA	0.996 (0.003)	0.005 (0.005)	0.996 (0.003)	0.005 (0.005)	0.158 (0.010)
	ULA	0.332 (0.020)	0.035 (0.001)	0.360 (0.018)	0.034 (0.001)	0.905 (0.001)
	PMD	0.712 (0.034)	0.633 (0.033)	0.662 (0.038)	0.633 (0.033)	0.974 (0.002)
	SCCA	0.560 (0.033)	0.565 (0.030)	0.586 (0.032)	0.567 (0.030)	0.989 (0.001)

Table 2: Variable selection accuracy, measured by TPR and FPR, and the subspace estimation accuracy, measured by D , for Scenario 2 where p_3 varies. The reported are the average criteria, with the standard errors in the parenthesis, over 100 data replications.

6 Multimodal PET Analysis

6.1 Study and data description

We revisit the multimodal PET study introduced in Section 1.1. It is part of the ongoing Berkeley Aging Cohort Study that targets Alzheimer’s disease (AD) as well as normal aging. AD is an irreversible neurodegenerative disorder and the leading form of dementia. It is characterized by progressive impairment of cognitive and memory functions, then loss of bodily functions, and ultimately death. AD and related dementia currently affects more than 10% of adults aged 65 or older, and the prevalence is continuously growing. It has now become an international imperative to understand, diagnose, and treat this disorder (Alzheimer’s Association, 2020).

The data consist of $n = 81$ elderly subjects, with the average age 77.5 years, and the standard deviation 6.2 years. For each subject, three types of neuroimages were acquired, including

n	Method	TPR-1	FPR-1	TPR-2	FPR-2	D
60	GLAA	0.606 (0.025)	0.048 (0.008)	0.664 (0.027)	0.154 (0.021)	0.743 (0.015)
	ULA	0.410 (0.022)	0.031 (0.001)	0.362 (0.018)	0.160 (0.004)	0.920 (0.004)
	PMD	0.498 (0.040)	0.486 (0.036)	0.552 (0.039)	0.466 (0.036)	0.957 (0.004)
	SCCA	0.604 (0.023)	0.059 (0.012)	0.688 (0.023)	0.643 (0.017)	0.968 (0.002)
80	GLAA	0.638 (0.027)	0.018 (0.002)	0.738 (0.025)	0.137 (0.027)	0.662 (0.021)
	ULA	0.550 (0.021)	0.024 (0.001)	0.412 (0.018)	0.147 (0.005)	0.895 (0.004)
	PMD	0.494 (0.038)	0.441 (0.034)	0.502 (0.038)	0.429 (0.034)	0.953 (0.004)
	SCCA	0.672 (0.026)	0.665 (0.016)	0.716 (0.025)	0.718 (0.019)	0.966 (0.003)
100	GLAA	0.820 (0.022)	0.013 (0.004)	0.848 (0.020)	0.060 (0.016)	0.483 (0.024)
	ULA	0.686 (0.019)	0.017 (0.001)	0.534 (0.021)	0.117 (0.005)	0.870 (0.004)
	PMD	0.510 (0.035)	0.476 (0.032)	0.560 (0.036)	0.442 (0.033)	0.947 (0.004)
	SCCA	0.702 (0.027)	0.677 (0.021)	0.732 (0.025)	0.714 (0.024)	0.961 (0.003)
120	GLAA	0.896 (0.018)	0.004 (0.001)	0.914 (0.018)	0.010 (0.003)	0.350 (0.021)
	ULA	0.802 (0.017)	0.010 (0.001)	0.622 (0.018)	0.094 (0.004)	0.850 (0.003)
	PMD	0.576 (0.035)	0.564 (0.032)	0.662 (0.035)	0.530 (0.032)	0.941 (0.004)
	SCCA	0.640 (0.030)	0.657 (0.024)	0.708 (0.028)	0.705 (0.022)	0.970 (0.003)
160	GLAA	0.990 (0.004)	0.001 (0.000)	0.984 (0.005)	0.002 (0.001)	0.209 (0.012)
	ULA	0.920 (0.011)	0.004 (0.001)	0.732 (0.016)	0.067 (0.004)	0.812 (0.003)
	PMD	0.610 (0.037)	0.570 (0.034)	0.652 (0.038)	0.544 (0.035)	0.944 (0.004)
	SCCA	0.626 (0.031)	0.651 (0.024)	0.698 (0.029)	0.0691 (0.024)	0.969 (0.003)

Table 3: Variable selection accuracy, measured by TPR and FPR, and the subspace estimation accuracy, measured by D , for Scenario 3 where n varies. The reported are the average criteria, with the standard errors in the parenthesis, over 100 data replications.

a Pittsburgh Compound B (PiB) PET scan that measures amyloid-beta protein, an AV-1451 PET scan that measures tau protein, and a 1.5T structural MRI scan that was used for coregistration. Both PET images have been preprocessed. Specifically, for PiB PET, the images were attenuation corrected, and reconstructed using an ordered subset expectation maximization algorithm with weighted attenuation and scatter correction. Native-space voxel-wise distribution volume ratio images were generated using Logan graphical analysis, with 35-90 min post-injection and cerebellar grey matter reference region (Logan et al., 1996). For AV-1451 PET, the images were synthesized and reconstructed in a similar fashion as PiB imaging. Native-space standardized uptake value ratio images were generated, with 80-100 min post-injection and inferior cerebellar grey matter reference region. MRI images were normalized to the FSL MNI152 2mm space template using Advanced Normalization Tools and a study-specific intermediate template (Lockhart et al., 2017). Native-space PET images were both coregistered to each participant’s MRI image.

Transformations were concatenated and applied to the coregistered AV-1451 and PiB PET images to generate MNI-space PET images. Moreover, we created and applied a mask representing voxels likely to accumulate cortical amyloid and tau pathology. To do this, we intersected a cortical brain mask from the Automated Anatomical Labeling atlas (Tzourio-Mazoyer et al., 2002), with a mask of high-probability grey matter voxels from the SPM12 tissue probability map. It was also masked to include only voxels where the coefficient of variation in the signal across participants in either PET modality was ≤ 0.5 , and the mean signal across participants was ≥ 0.8 . From a FreeSurfer segmentation of the MNI152 template structural MRI, a set of MNI-space testing regions were created that encompass Braak I-IV stage regions for AV-1451, and Braak I-V stage regions for PiB, excluding basal ganglia and thalamus (Schöll et al., 2016). These testing regions have been designed to focus on areas of possible tau and $A\beta$ accumulations. MNI-space PiB and AV-1451 PET images were masked by this cortical mask before data analysis. This results in $p_1 = 60$ regions-of-interest for amyloid-beta PET, and $p_2 = 26$ regions for tau-PET.

6.2 Analyses and results

One of the primary goals of this study is to identify brain regions where the association of amyloid-beta and tau changes the most as age varies, and to further understand this association change. We cast this problem in the framework of liquid association analysis. Let $\mathbf{X} \in \mathbb{R}^{60}$, $\mathbf{Y} \in \mathbb{R}^{26}$ denote the amyloid-beta accumulation and tau accumulation in various brain regions, respectively, and $Z \in \mathbb{R}$ denote the subject’s age. We first log-transform each variable in \mathbf{X} and \mathbf{Y} , and standardize \mathbf{X} , \mathbf{Y} and Z marginally. We then apply the proposed generalized liquid association analysis (GLAA) method to this data.

After obtaining the two estimated linear combinations $\widehat{\Gamma}_1^\top \mathbf{X}$ and $\widehat{\Gamma}_2^\top \mathbf{Y}$, we plot them as the value of Z changes. We divide the interval of Z into six equal-sized intervals with overlaps, then draw the scatterplot of $\widehat{\Gamma}_2^\top \mathbf{Y}$ versus $\widehat{\Gamma}_1^\top \mathbf{X}$ within each interval. We also add a fitted linear regression line in each panel to reflect the correlation between $\widehat{\Gamma}_1^\top \mathbf{X}$ and $\widehat{\Gamma}_2^\top \mathbf{Y}$. Figure 1 shows the trellis plots, where the stripe at the top of each panel represents the range of Z it covers. It is interesting to see from the GLAA estimation, the correlation between $\Gamma_1^\top \mathbf{X}$ and $\Gamma_2^\top \mathbf{Y}$ changes from negative to positive gradually, as the age variable Z increases. This may be due to different deposition patterns of amyloid-beta and tau. In particular, amyloid-beta plaques are detectable in the brain many years before dementia onset, while tau neurofibrillary tangles aggregate specif-

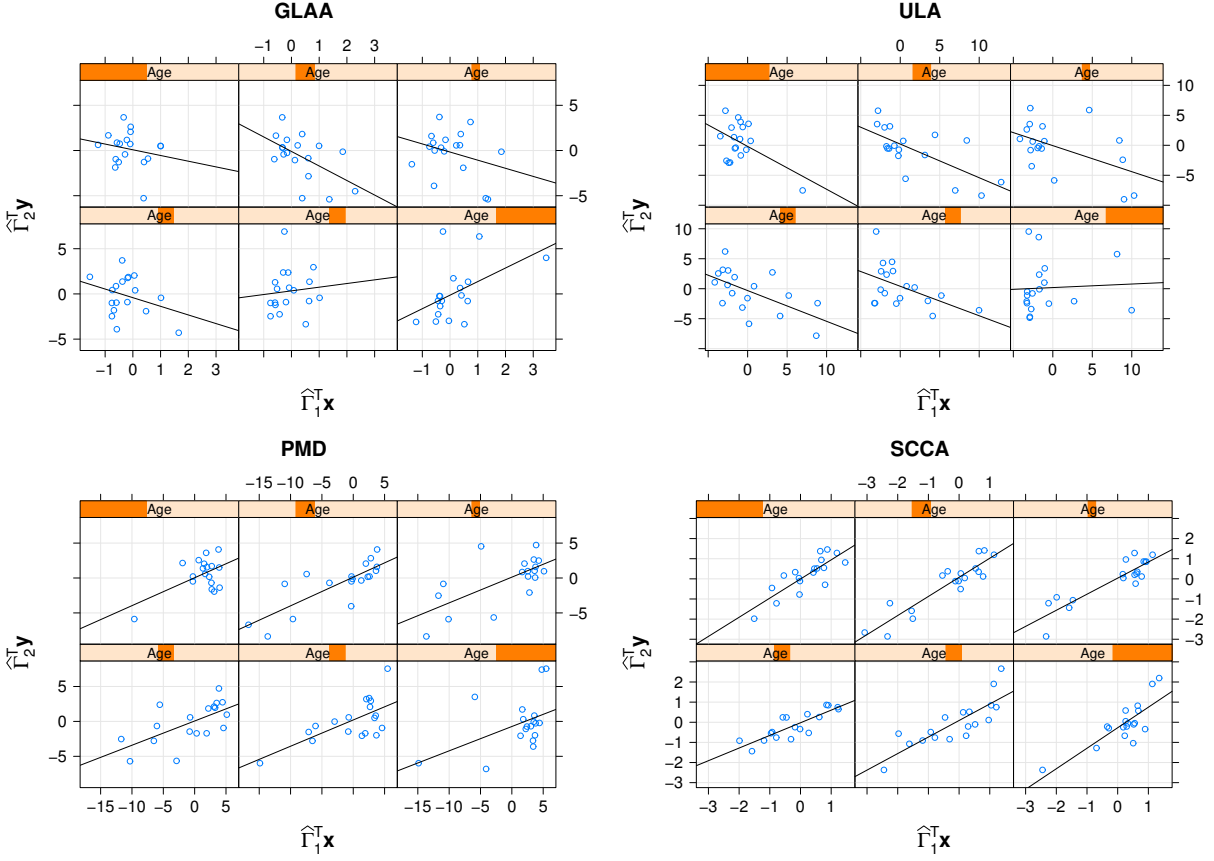


Figure 1: Trellis plots of the estimated linear combinations $\hat{\Gamma}_2^\top \mathbf{Y}$ versus $\hat{\Gamma}_1^\top \mathbf{X}$ as \mathbf{Z} varies. Each panel represents an interval of \mathbf{Z} , with a linear regression line added. The methods under comparison are: generalized liquid association analysis (GLAA), univariate liquid association (ULA), penalized matrix decomposition (PMD), and sparse canonical correlation analysis (SCCA).

ically in the medial temporal lobes in normal aging. The spread of tau out of medial temporal lobes and into the surrounding isocortex at elder age coincides with cognitive impairment, and the process is hypothesized to be potentiated or accelerated by the presence of amyloid-beta (He et al., 2018; Vogel et al., 2020). The change from a negative association in early years to a positive association in later years between amyloid-beta and tau found by our GLAA method may offer some support to this hypothesis. As a comparison, no clear changing pattern is observed from the other three estimation methods.

Next, we examine more closely the brain regions identified by GLAA that demonstrate dynamic association patterns. Figure 2 plots the loadings of the estimated $\hat{\Gamma}_1$ and $\hat{\Gamma}_2$, where the indices of non-zero loadings correspond to the selected regions. The number of non-zero loading

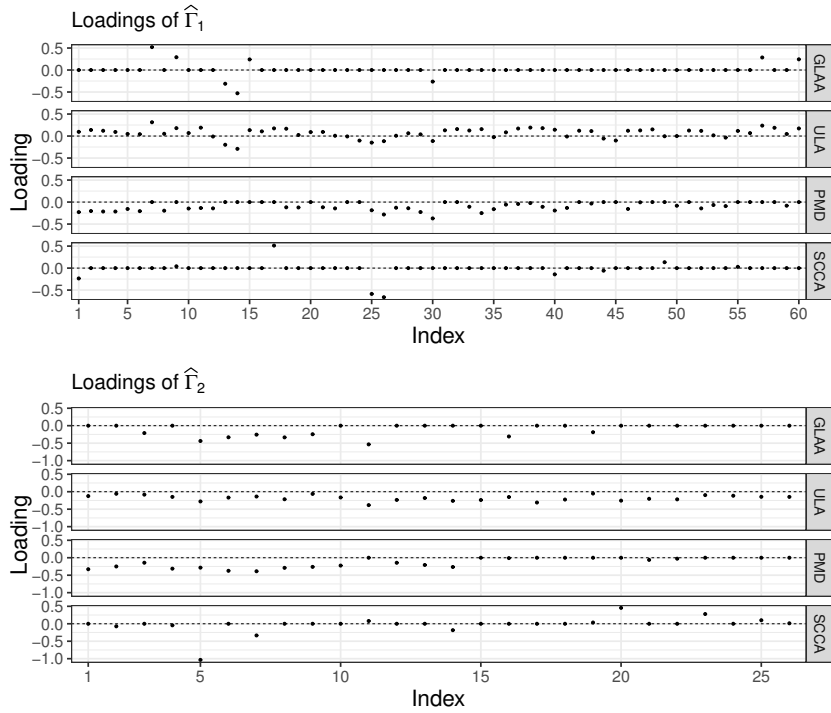


Figure 2: Estimated loadings in $\hat{\Gamma}_1$ and $\hat{\Gamma}_2$. The number of non-zero loading entries estimated by GLAA, ULA, PMD, SCCA are 8, 60, 37, 9 for $\hat{\Gamma}_1$, and 9, 26, 16, 11 for $\hat{\Gamma}_2$, respectively.

entries estimated by GLAA, ULA, PMD, SCCA are 8, 60, 37, 9 for $\hat{\Gamma}_1$, and 9, 26, 16, 11 for $\hat{\Gamma}_2$, respectively. Note that, the ULA method does not deal with variable selection, and for the real data, no information on the true sparsity level is known, so its estimated loadings are non-sparse. Moreover, the PMD method yields a large number of non-zero estimates, making the interpretation difficult. The SCCA method selects about the same number of non-zero regions as GLAA, but the selected regions are less meaningful and are difficult to interpret.

Table 4 reports the identified brain regions by GLAA for amyloid-beta and tau, respectively, while Figure 3 visualizes those regions on a template brain using BrainNet Viewer (Xia et al.,

Modality	Identified regions				
amyloid-beta	Entorhinal R	Entorhinal L	Hippocampus R	Hippocampus L	Amygdala R
	Orbitofrontal L	Posterior Cingulate L	Middle Frontal R		
tau	Entorhinal R	Entorhinal L	Hippocampus R	Parahippocampal R	Fusiform L
	Middle Temporal R	Middle Temporal L	Insula L	Rostral Anterior Cingulate R	

Table 4: Identified brain region names for amyloid-beta and tau by GLAA. Regions in the left hemisphere are denoted by “L”, and regions in the right hemisphere are denoted by “R”.

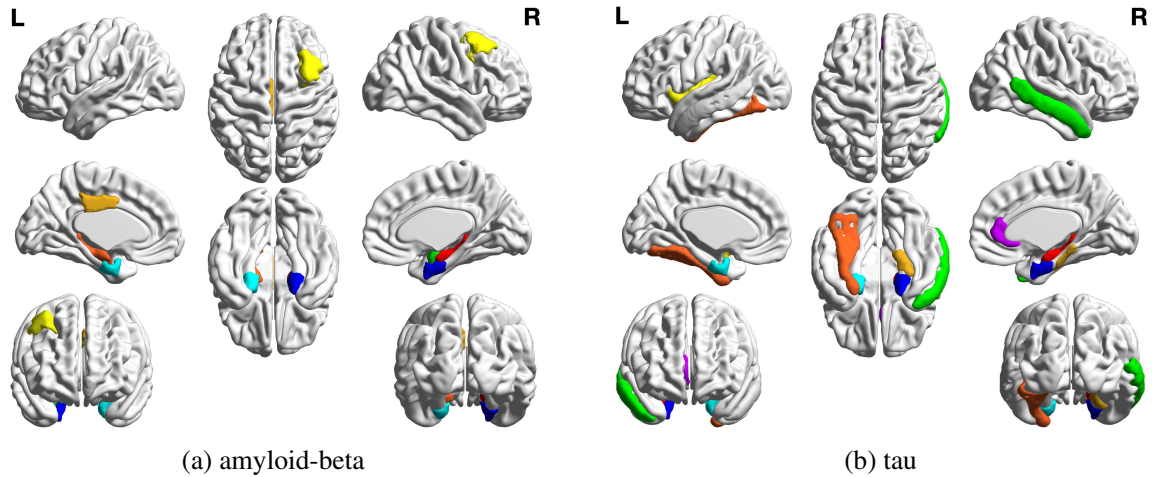


Figure 3: Identified brain regions for amyloid-beta and tau by GLAA.

2013). Many of these regions are known to be closely related to AD, and the dynamic associations between amyloid-beta and tau of those regions reveal interesting and new insights. Particularly, for both amyloid-beta and tau, the identified regions include hippocampus and entorhinal cortex. The hippocampus is a major component of the human brain located in the medial temporal lobe, and is functionally involved in response inhibition, episodic memory, and spatial cognition. It is one of the first brain regions to suffer damage from AD, and is the best established biomarker for AD (Jack et al., 2011). The entorhinal cortex is a brain area also located in the medial temporal lobes, and functions as a hub in a widespread network for memory, navigation and the perception of time. The entorhinal cortex is the main interface between the hippocampus and neocortex, and together with hippocampus, plays an important role in memories. Atrophy in the entorhinal cortex has been consistently reported in AD (Pini et al., 2016). Moreover, animal models have suggested that neurofibrillary tangles of tau first appear in the entorhinal cortex, then spread to the hippocampus (Cho et al., 2016). For amyloid-beta, other identified regions include amygdala, orbitofrontal cortex, posterior cingulate cortex and areas of middle frontal cortices. The amygdala locates within the temporal lobes of the brain, and performs a primary role in the processing of memory, decision-making and emotional responses. Amygdala atrophy is found prominent in early AD (Poulin et al., 2011). The orbitofrontal cortex locates in the frontal lobes of the brain, and is involved in the cognitive process of decision-making, while the posterior cingulate cortex is part of the cingulate cortex, is one of the most metabolically active brain regions, and is linked to emotion and memory. Atrophy of both regions and the middle frontal

cortices have all been found associated with AD (Van Hoesen et al., 2000; Minoshima et al., 1997; Pini et al., 2016). For tau, other identified regions include parahippocampal gyrus, middle temporal gyrus, fusiform, insula, and rostral anterior cingulate cortex. The parahippocampal gyrus is a region surrounding the hippocampus, and plays an important role in memory encoding and retrieval. Atrophy in the parahippocampal gyrus has been identified as an early biomarker of AD (Echavarri et al., 2011). Middle temporal gyrus is located on the temporal lobes, and is connected with processes of recognition of known faces and accessing word meaning while reading. The fusiform is located above the parahippocampal gyrus, and is linked with various neural pathways related to recognition. The insula is a portion of the cerebral cortex folded deep within the lateral sulcus, and is involved in consciousness and diverse functions linked to emotion. The rostral anterior cingulate cortex is frontal part of the cingulate cortex, and is involved in higher-level functions, such as attention allocation, decision-making and emotion. There have been evidences suggesting the associations between these regions and AD (Convit et al., 2000; Pini et al., 2016).

In summary, GLAA identifies interesting dynamic association patterns among a number of important brain regions between amyloid-beta and tau as age increases. Moreover, GLAA provides a useful dimension reduction tool to help visualize such patterns.

7 Discussion

In this article, we propose generalized liquid association analysis, which offers a new angle to study three-way associations among random variables, and is particularly useful for multimodal integrative data analysis. Next, we discuss some potential extensions.

First, we begin with the situation when there is a univariate and categorical Z , whereas the analysis so far has primarily concentrated on the case when each variable in \mathbf{Z} is continuous. In general, it remains an open question on how to define liquid association for a categorical variable, since the function $g(z)$ is no longer differentiable for a categorical Z . For a binary $Z \in \{0, 1\}$, we propose to replace the derivative of the conditional mean function with the absolute change in the conditional means across the two groups, i.e., $LA(X, Y|Z) = |E(XY|Z = 1) - E(XY|Z = 0)|$, where the absolute value is used because the class labels are interchangeable. This naturally fits the original interpretation of LA. Similarly, for a categorical or ordinal $Z \in \{1, \dots, K\}$, we

can use the weighted sum of pairwise absolute mean difference between the pairs of groups. Accordingly, the liquid association of \mathbf{X} and \mathbf{Y} given \mathbf{Z} is defined as a $p_1 \times p_2$ matrix.

Next, for a multivariate mixed type \mathbf{Z} , we first organize $\mathbf{Z} = (\mathbf{Z}_1, \mathbf{Z}_2)^T$ to separate the continuous variables, $\mathbf{Z}_1 = (Z_1, \dots, Z_q)^T \in \mathbb{R}^q$, from the categorical variables, $\mathbf{Z}_2 = (Z_{q+1}, \dots, Z_{p_3})^T \in \mathbb{R}^{p_3-q}$. Directly imposing a low-dimensional structure on entire \mathbf{Z} would lead to difficulty in interpretation. Alternatively, we propose a dimension reduction approach, by recognizing the reduction on \mathbf{Z} in model (1) is indeed a sufficient dimension reduction model. Specifically, when \mathbf{Z} is continuous, by model (1), we have $\mathbf{g}(\mathbf{Z}) = \mathbf{g}(\mathbf{P}_S \mathbf{Z})$, where $S = \text{span}(\Gamma_3)$. Therefore, $\mathbf{g}(\mathbf{Z}) \perp\!\!\!\perp \mathbf{Z} | \mathbf{P}_S \mathbf{Z}$. This leads to a sufficient dimension reduction model of \mathbf{Z} for the conditional mean function $g(\mathbf{Z}) = \mathbb{E}(\mathbf{X}\mathbf{Y}^T | \mathbf{Z})$, in the sense that all the mean information of the regression of the matrix response $\mathbf{X}\mathbf{Y}^T$ given the predictor vector \mathbf{Z} is fully captured by the linear combinations $\Gamma_3^T \mathbf{Z}$. As such, model (1) can be viewed as a generalization of the notion of sufficient mean reduction (Cook and Li, 2002). Now for the mixed type $\mathbf{Z} = (\mathbf{Z}_1^T, \mathbf{Z}_2^T)^T$, we adopt the idea of partial dimension reduction (Chiaromonte et al., 2002), or groupwise dimension reduction (Li et al., 2010), and estimate the subspace $S \subseteq \mathbb{R}^q$ such that $\mathbf{g}(\mathbf{Z}) \perp\!\!\!\perp \mathbf{Z} | (\mathbf{P}_S \mathbf{Z}_1, \mathbf{Z}_2)$.

Finally, from the simulation results in Table 2, we observe that, the higher the dimension of \mathbf{Z} , the more challenging the problem becomes. We believe it is possible to employ an alternative modeling strategy such as Chen et al. (2011) when the dimension of \mathbf{Z} is ultrahigh. This is also true when the scientific interest is to select important variables in \mathbf{Z} , while our current interest concentrates on selection of variables in \mathbf{X} and \mathbf{Y} , but not in \mathbf{Z} . We leave the pursuit of this line of research as our future work.

References

- Abid, A., Zhang, M. J., Bagaria, V. K., and Zou, J. (2018). Exploring patterns enriched in a dataset with contrastive principal component analysis. *Nature communications*, 9(1):1–7.
- Alzheimer’s Association (2020). 2020 Alzheimer’s disease facts and figures. *Alzheimer’s & Dementia*, 16(3):391–460.
- Bi, X., Qu, A., and Shen, X. (2018). Multilayer tensor factorization with applications to recommender systems. *The Annals of Statistics*, 46(6B):3308–3333.

- Bi, X., Tang, X., Yuan, Y., Zhang, Y., and Qu, A. (2020). Tensor in statistics. *Annual Review of Statistics and Its Application*, to appear.
- Braak, H. and Braak, E. (1991). Neuropathological staging of alzheimer-related changes. *Acta Neuropathologica*, 82(4):239–259.
- Chen, J., Xie, J., and Li, H. (2011). A penalized likelihood approach for bivariate conditional normal models for dynamic co-expression analysis. *Biometrics*, 67(1):299–308.
- Chiaromonte, F., Cook, R. D., Li, B., et al. (2002). Sufficient dimensions reduction in regressions with categorical predictors. *The Annals of Statistics*, 30(2):475–497.
- Cho, H., Choi, J. Y., Hwang, M. S., Kim, Y. J., Lee, H. M., Lee, H. S., Lee, J. H., Ryu, Y. H., Lee, M. S., and Lyoo, C. H. (2016). In vivo cortical spreading pattern of tau and amyloid in the alzheimer disease spectrum. *Annals of Neurology*, 80(2):247–258.
- Convit, A., [de Asis], J., [de Leon], M., Tarshish, C., Santi, S. D., and Rusinek, H. (2000). Atrophy of the medial occipitotemporal, inferior, and middle temporal gyri in non-demented elderly predict decline to alzheimers disease. *Neurobiology of Aging*, 21(1):19–26.
- Cook, R. D. (1998). Principal hessian directions revisited. *Journal of the American Statistical Association*, 93(441):84–94.
- Cook, R. D. (2007). Fisher lecture: Dimension reduction in regression. *Statistical Science*, 22(1):1–26.
- Cook, R. D. and Li, B. (2002). Dimension reduction for conditional mean in regression. *The Annals of Statistics*, 30(2):455–474.
- Echavarri, C., Aalten, P., Uylings, H., Jacobs, H., Visser, P., Gronenschild, E., Verhey, F., and Burgmans, S. (2011). Atrophy in the parahippocampal gyrus as an early biomarker of alzheimer’s disease. *Brain Structure & Function*, 215:265–271.
- Fornito, A., Zalesky, A., and Breakspear, M. (2013). Graph analysis of the human connectome: Promise, progress, and pitfalls. *NeuroImage*, 80:426–444.
- Gao, C., Ma, Z., Ren, Z., and Zhou, H. H. (2015). Minimax estimation in sparse canonical correlation analysis. *The Annals of Statistics*, 43:2168–2197.

- He, Z., Guo, J. L., McBride, J. D., Narasimhan, S., Kim, H., Changolkar, L., Zhang, B., Gathagan, R. J., Yue, C., Dengler, C., Stieber, A., Nitla, M., Coulter, D. A., Abel, T., Brunden, K. R., Trojanowski, J. Q., and Lee, V. M.-Y. (2018). Amyloid-beta plaques enhance alzheimer’s brain tau-seeded pathologies by facilitating neuritic plaque tau aggregation. *Nature Medicine*, 24(1):29–38.
- Ho, Y.-Y., Parmigiani, G., Louis, T. A., and Cope, L. M. (2011). Modeling liquid association. *Biometrics*, 67(1):133–141.
- Jack, C. R., Barkhof, F., Bernstein, M. A., Cantillon, M., Cole, P. E., DeCarli, C., Dubois, B., Duchesne, S., Fox, N. C., Frisoni, G. B., Hampel, H., Hill, D. L., Johnson, K., Mangin, J.-F., Scheltens, P., Schwarz, A. J., Sperling, R., Suhy, J., Thompson, P. M., Weiner, M., and Foster, N. L. (2011). Steps to standardization and validation of hippocampal volumetry as a biomarker in clinical trials and diagnostic criterion for alzheimer’s disease. *Alzheimer’s & Dementia*, 7(4):474–485.e4.
- Kang, J., Bowman, F. D., Mayberg, H., and Liu, H. (2016). A depression network of functionally connected regions discovered via multi-attribute canonical correlation graphs. *NeuroImage*, 141:431–441.
- Kolda, T. G. and Bader, B. W. (2009). Tensor decompositions and applications. *SIAM review*, 51(3):455–500.
- Li, B. (2018). *Sufficient Dimension Reduction: Methods and Applications with R*. Chapman & Hall/CRC Monographs on Statistics and Applied Probability. CRC Press.
- Li, G. and Gaynanova, I. (2018). A general framework for association analysis of heterogeneous data. *The Annals of Applied Statistics*, 12(3):1700–1726.
- Li, G. and Jung, S. (2017). Incorporating covariates into integrated factor analysis of multi-view data. *Biometrics*, 73(4):1433–1442.
- Li, K.-C. (1992). On principal hessian directions for data visualization and dimension reduction: Another application of stein’s lemma. *Journal of the American Statistical Association*, 87(420):1025–1039.
- Li, K.-C. (2002). Genome-wide coexpression dynamics: theory and application. *Proceedings of the National Academy of Sciences*, 99(26):16875–16880.

- Li, K.-C., Liu, C.-T., Sun, W., Yuan, S., and Yu, T. (2004). A system for enhancing genome-wide coexpression dynamics study. *Proceedings of the National Academy of Sciences*, 101(44):15561–15566.
- Li, L., Li, B., and Zhu, L.-X. (2010). Groupwise dimension reduction. *Journal of the American Statistical Association*, 105(491):1188–1201.
- Liu, J. S. (1994). Siegel’s formula via stein’s identities. *Statistics & Probability Letters*, 21(3):247–251.
- Lock, E. F., Hoadley, K. A., Marron, J. S., and Nobel, A. B. (2013). Joint and individual variation explained (jive) for integrated analysis of multiple data types. *The annals of applied statistics*, 7(1):523.
- Lockhart, S. N., Schöll, M., Baker, S. L., Ayakta, N., Swinnerton, K. N., Bell, R. K., Mellinger, T. J., Shah, V. D., O’Neil, J. P., Janabi, M., and Jagust, W. J. (2017). Amyloid and tau PET demonstrate region-specific associations in normal older people. *NeuroImage*, 150:191–199.
- Logan, J., Fowler, J. S., Volkow, N. D., Wang, G.-J., Ding, Y.-S., and Alexoff, D. L. (1996). Distribution volume ratios without blood sampling from graphical analysis of pet data. *Journal of Cerebral Blood Flow & Metabolism*, 16:834–840.
- Mai, Q. and Zhang, X. (2019). An iterative penalized least squares approach to sparse canonical correlation analysis. *Biometrics*, 75(3):734–744.
- Minoshima, S., Giordani, B., Berent, S., Frey, K. A., Foster, N. L., and Kuhl, D. E. (1997). Metabolic reduction in the posterior cingulate cortex in very early alzheimer’s disease. *Annals of Neurology*, 42(1):85–94.
- Nathoo, F. S., Kong, L., and Zhu, H. (2017). Inference on high-dimensional differential correlation matrix. *arXiv preprint arXiv:1707.07332*.
- Pini, L., Pievani, M., Bocchetta, M., Altomare, D., Bosco, P., Cavedo, E., Galluzzi, S., Marizzoni, M., and Frisoni, G. B. (2016). Brain atrophy in alzheimers disease and aging. *Ageing Research Reviews*, 30:25–48. Brain Imaging and Aging.
- Poulin, S. P., Dautoff, R., Morris, J. C., Barrett, L. F., and Dickerson, B. C. (2011). Amygdala atrophy is prominent in early alzheimer’s disease and relates to symptom severity. *Psychiatry Research: Neuroimaging*, 194(1):7–13.

- Richardson, S., Tseng, G. C., and Sun, W. (2016). Statistical methods in integrative genomics. *Annual Review of Statistics and Its Application*, 3:181–209.
- Rudelson, M. and Vershynin, R. (2010). Non-asymptotic theory of random matrices: extreme singular values. In *Proceedings of the International Congress of Mathematicians 2010 (ICM 2010) (In 4 Volumes) Vol. I: Plenary Lectures and Ceremonies Vols. II–IV: Invited Lectures*, pages 1576–1602. World Scientific.
- Schöll, M., Lockhart, S., Schonhaut, D., O’Neil, J., Janabi, M., Ossenkoppele, R., Baker, S., Vogel, J., Faria, J., Schwimmer, H., Rabinovici, G., and Jagust, W. (2016). PET imaging of tau deposition in the aging human brain. *Neuron*, 89:971–982.
- Shen, R., Wang, S., and Mo, Q. (2013). Sparse integrative clustering of multiple omics data sets. *Ann. Appl. Stat.*, 7(1):269–294.
- Shu, H., Wang, X., and Zhu, H. (2019). D-cca: A decomposition-based canonical correlation analysis for high-dimensional datasets. *Journal of the American Statistical Association*, pages 1–29.
- Stein, C. M. (1981). Estimation of the mean of a multivariate normal distribution. *The annals of Statistics*, pages 1135–1151.
- Tang, C. Y., Fang, E. X., and Dong, Y. (2020). High-dimensional interactions detection with sparse principal hessian matrix. *Journal of Machine Learning Research*, 21(19):1–25.
- Tang, X., Bi, X., and Qu, A. (2019). Individualized multilayer tensor learning with an application in imaging analysis. *Journal of the American Statistical Association*, pages 1–26.
- Tzourio-Mazoyer, N., Landeau, B., Papathanassiou, D., Crivello, F., Etard, O., Delcroix, N., Mazoyer, B., and Joliot, M. (2002). Automated anatomical labeling of activations in SPM using a macroscopic anatomical parcellation of the MNI MRI single-subject brain. *NeuroImage*, 15:273–289.
- Uludag, K. and Roebroeck, A. (2014). General overview on the merits of multimodal neuroimaging data fusion. *NeuroImage*, 102, Part 1:3 – 10.
- Van Hoesen, G. W., Parvizi, J., and Chu, C.-C. (2000). Orbitofrontal Cortex Pathology in Alzheimer’s Disease. *Cerebral Cortex*, 10(3):243–251.

- Vogel, J. W., Iturria-Medina, Y., and et al. (2020). Spread of pathological tau proteins through communicating neurons in human alzheimer’s disease. *Nature Communications*, 11(1):2612.
- Wainwright, M. J. (2019). *High-dimensional statistics: A non-asymptotic viewpoint*, volume 48. Cambridge University Press.
- Witten, D. M., Tibshirani, R., and Hastie, T. (2009). A penalized matrix decomposition, with applications to sparse principal components and canonical correlation analysis. *Biostatistics*, 10(3):515–534.
- Xia, M., Wang, J., and He, Y. (2013). Brainnet viewer: A network visualization tool for human brain connectomics. *PLOS ONE*, 8(7):1–15.
- Xia, Y., Li, L., Lockhart, S. N., and Jagust, W. J. (2019). Simultaneous covariance inference for multimodal integrative analysis. *Journal of the American Statistical Association*, 0(0):1–13.
- Yang, D., Ma, Z., and Buja, A. (2016). Rate optimal denoising of simultaneously sparse and low rank matrices. *The Journal of Machine Learning Research*, 17(1):3163–3189.
- Yu, T. (2018). A new dynamic correlation algorithm reveals novel functional aspects in single cell and bulk rna-seq data. *PLOS Computational Biology*, 14:1–22.
- Yu, Y., Wang, T., and Samworth, R. J. (2015). A useful variant of the davis–kahan theorem for statisticians. *Biometrika*, 102(2):315–323.
- Zhang, A. and Han, R. (2019). Optimal sparse singular value decomposition for high-dimensional high-order data. *Journal of the American Statistical Association*, pages 1–34.
- Zhou, H., Li, L., and Zhu, H. (2013). Tensor regression with applications in neuroimaging data analysis. *Journal of the American Statistical Association*, 108:540–552.